The Influence of Microstructure on the Corrosion of Magnesium Alloy ZEK100

R. Matthew Asmussen,[‡] W. Jeffrey Binns, Pellumb Jakupi, and David Shoesmith*

ABSTRACT

The corrosion behavior of Mg alloy ZEK100 was investigated in water and in chloride-containing environments. The alloy is composed of an α-Mg matrix and a wide-spread dispersion of a Mg-Zn-Nd phase and Zr-rich particles. Potentiodynamic polarization measurements showed the corrosion resistance of the ZEK100 alloy improved with decreasing chloride content. Intermittent immersions in 0.16 wt% sodium chloride (NaCl) showed corrosion occurred preferentially by tracking along the surface, interlinking the secondary phase particles. Some of the particles acted as strong cathodes microgalvanically coupled to the α-Mg matrix. Of the three main types of secondary phase identified, i.e., Mg-Zn-Nd, Zr, and Fe-containing Zr particles, the latter were the dominant active cathodes. This was demonstrated by experiments in deionized water (18.2 MΩ cm) where the tracking of corrosion across the surface was absent and active cathodes could be identified by a small surrounding zone of corroded α-Mg and an accumulated dome of corrosion product over the top of the active particle.

KEY WORDS: corrosion, electron microscopy, magnesium alloys, rare earths

INTRODUCTION

Magnesium alloys are excellent candidates for inclusion in automobiles because they would reduce vehicle weight, leading to improved fuel efficiency and/ or more viable electric vehicles. Several factors limit a broad implementation of Mg alloys in automotive construction, however, including material and manufacturing costs, poor formability below 200°C, and poor corrosion resistance.[1-2] The lack of low temperature formability is especially of concern for sheet Mg alloys.[3] The ZEK100 Mg alloy, containing Zn for strength, rare earths (RE) for reduced texture, and Zr for grain refinement, has been shown to display improved low temperature forming properties making it a candidate for use in automobile construction as doors, deck lids, liftgate inner panels, and seat backs.[4]

The corrosion behavior of many common Mg alloys have been investigated,[5] with considerable attention being paid to the aluminum zinc (AZ)[6-8] and aluminum manganese (AM)-series of alloys.[9-13] The corrosion behavior of the ZEK100 alloy has not been as extensively analyzed, although its potential as a biomedical material has been investigated,[14-16] and its performance compared to that of other Mg alloys: voltametric measurements showed the alloy to be less corrosion resistant than the LAE 442, AE 42, and AZ 31 alloys[17] and below the AZ-series alloys and ZE 41 in a galvanic ranking of Mg alloys based on their corrosion potential (E_{CORR}).[18] Two recent studies used high resolution electron microscopy to investigate the nature and growth of surface films during corrosion of the similar ZE10A alloy.[19-20]

In this study, the role of alloying elements on the corrosion of ZEK100 was investigated. This was achieved using a combination of electrochemical and microscopic techniques similar to those successfully employed to investigate the role of microstructure in the corrosion of the AM50 Mg alloy.[21] Using this ap-

proach, the initiation and progression of corrosion can be tracked, and the features responsible for supporting the cathodic half reaction can be identified. Cathodic features in Mg materials are of topical interest because of their controlling influence on the corrosion of Mg alloys[22-25] and their important role in the enhanced hydrogen evolution observed on anodically polarized Mg.[26-28] In particular, the factors controlling the corrosion rate of ZEK100 and the distribution of corrosion damage have been investigated by comparing alloy behavior in solutions with different chloride concentrations.

EXPERIMENTAL

Sample Preparation

Rolled ZEK100 alloy sheets (F-temper) were cut into 1 cm by 1 cm by 2 mm samples and threaded on one side to allow electrical connection to external circuitry via a steel rod. The composition of the ZEK100 from the supplier is given in Table 1. All samples were mounted in Struers EpoFix™† so that only a single face of the sample was exposed to solution. The samples were ground successively with silicon carbide (SiC) papers of 800, 1200, 2400, and 4000 grit and then polished with a 3 μm diamond paste using ethanol/isopropanol as a lubricant. Samples were sonicated in methanol following each step. A final polish was applied using colloidal silica with ethylene glycol as a lubricant. Following this treatment, the sample was sonicated in methanol and dried in an Ar gas stream.

Instrumentation

Scanning electron microscopy (SEM) was performed in either secondary electron (SE) or backscattered electron (BSE) mode using either a LEO 440, Hitachi 3400-N variable pressure scanning electron microscope† or a LEO 1540 XB SEM/FIB. X-ray energy dispersive spectroscopy (XEDS) maps were obtained using Quartz One software®†. Optical stereo micrographs were collected using a Zeiss Lunar V12 microscope† equipped with an Axio 1.1 camera.†

Electrochemical Measurements

Electrochemical measurements were performed in a standard three-electrode glass cell with a saturated calomel reference electrode (SCE) and a Pt-plate counter electrode. Solutions were prepared using reagent grade NaCl (99% assay, [Caledon Labs, Georgetown, ON]) and deionized water (18.2 MΩ cm).

Electrochemical control was provided by a Solartron 1480 MultiStat®† potentiodynamic polarization (PDP) scans were performed, in triplicate, after first allowing the sample to acquire a stable corrosion potential (E_{CORR}) for 1 h and then scanning the potential at 0.167 mV/s from 150 mV below the E_{CORR} to either

TABLE 1
Composition of the ZEK100 Alloy Used in this Study (wt%)

Mg	Zn	Zr	Nd	Ce	La	Fe
Bal.	1.34	0.230	0.182	0.008	0.001	<0.005

−1.2 V or until a current density of 0.1 mA/cm² was reached. This current maximum was set to limit damage to the sample surface.

Intermittent Immersion Experiments

Polished ZEK100 samples were first imaged with SEM/XEDS to locate an area of interest (AOI) whose position was then recorded relative to a scratch at the edge of the sample surface. Immersions were performed in naturally aerated 1.6 wt% NaCl, 0.16 wt% NaCl, and deionized water by suspending the polished surface in the solution using a stainless steel rod. Following a set duration of exposure, the sample was removed, rinsed with deionized water and dried in an Ar stream. The AOI was located and imaged by SEM, and then reimmersed in the solution for a further exposure period. A series of such immersions, followed by imaging, was performed. On completion of this series, the accumulated corrosion product was removed through a 20 s immersion in gently agitated 1 M chromium (VI) oxide (CrO_3). Focused-ion beam (FIB) analyses of the samples were performed using a Ga ion beam.

RESULTS

Surface Imaging

An AOI on the polished ZEK100 surface is shown in the SEM micrograph in Figure 1(a), and Figure 1(b) shows the SEM micrograph of the particle marked with the blue arrow (labelled [b]) in Figure 1(a). Two sites were analyzed by XEDS: Site 1 outside the particle and Site 2 within it. The XEDS spectra in Figure 1(d), show the matrix (Site 1) was predominantly Mg, while the particle at Site 2 was composed of Zr. The SEM micrograph of the particle marked with the red arrow (labelled [c]) in Figure 1(a) is shown in Figure 1(c), and the XEDS spectrum reveals that it contains Zn and Nd. This particle is possibly a form of the tertiary phase (T-phase) which has been identified as present in RE-containing Mg-Zn alloys.[29] No Mg signal was observed for Site 2, suggesting that the Mg signal from the similarly sized particle in Figure 1(c) is an indication of the Mg content of that particle, not a signal from the surrounding matrix as a result of the excitation volume of the electron beam.

Electrochemical Effect of Chloride Ion Concentration

The effect of varying the chloride ion concentration of the solution on the electrochemical behavior
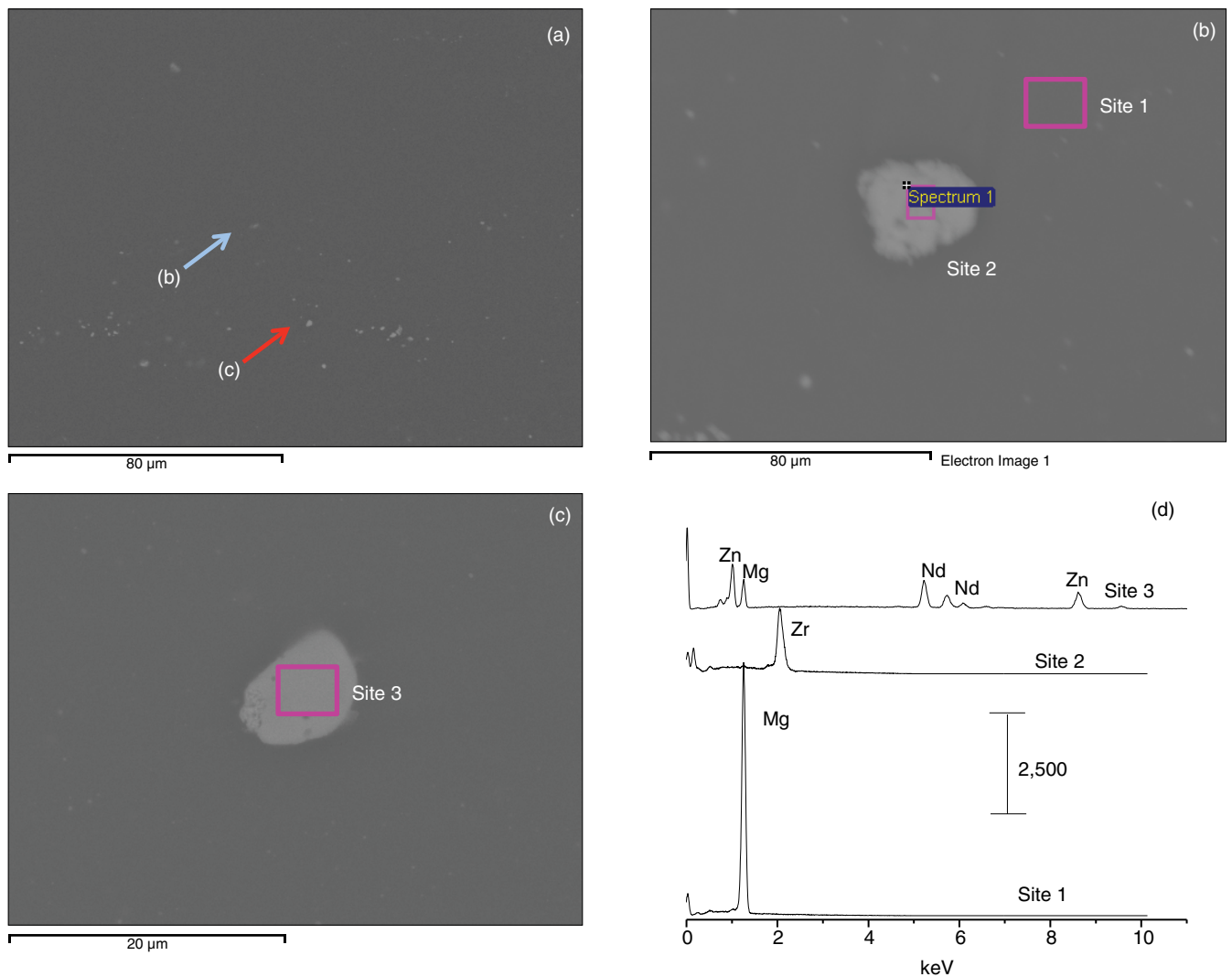
FIGURE 1. *(a) BSE SEM micrograph of an AOI with arrow indicating two particles; (b) BSE SEM micrograph of the particle marked with arrow "b" (blue) in (a); (c) SEM micrograph of the particle marked with arrow "c" (red) in (a); (d) the XEDS spot analyses of the locations numbered in the SEM images in (a).*

of ZEK100 was studied using PDP measurements, Figure 2(a). While the cathodic behavior was only marginally influenced by the chloride concentration, significant differences in anodic behavior were observed. In 1.6 wt% NaCl, an increase in current density occurred at –1.55 V almost immediately after the net current becomes anodic at –1.57 V, indicating rapid oxide/hydroxide film breakdown and the establishment of an extremely active surface. On reducing the chloride content to 0.16 wt% NaCl, similar behavior, with a slightly decreased reactivity was observed. The onset of film breakdown, leading to an extremely reactive surface and high measured currents, did not occur until the potential exceeded –1.45 V. When the chloride concentration is further reduced to 0.016 wt% NaCl, a significant potential range within which the alloy is partially protected is observed, and the

establishment of a reactive surface is delayed until the potential is > –1.38 V. In addition, the magnitude of the active current (i.e., the current observed at potentials positive to the breakdown potential) is significantly reduced as the chloride concentration is decreased. To ensure that the real influence of chloride content was observed, iR-compensated polarization curves, produced using the linear fit method, are shown in Figure 2(b). The iR-compensated PDP curves demonstrate that the differences in behaviors can be attributed to the influence of chloride concentration, especially the rapid increase in anodic current at positive potentials. As the chloride concentration is decreased, the potential for film breakdown shifts from E_{CORR} + 40 mV (1.6 wt% NaCl) to E_{CORR} + 88 mV (0.016 wt%), where E_{CORR} is the corrosion potential.
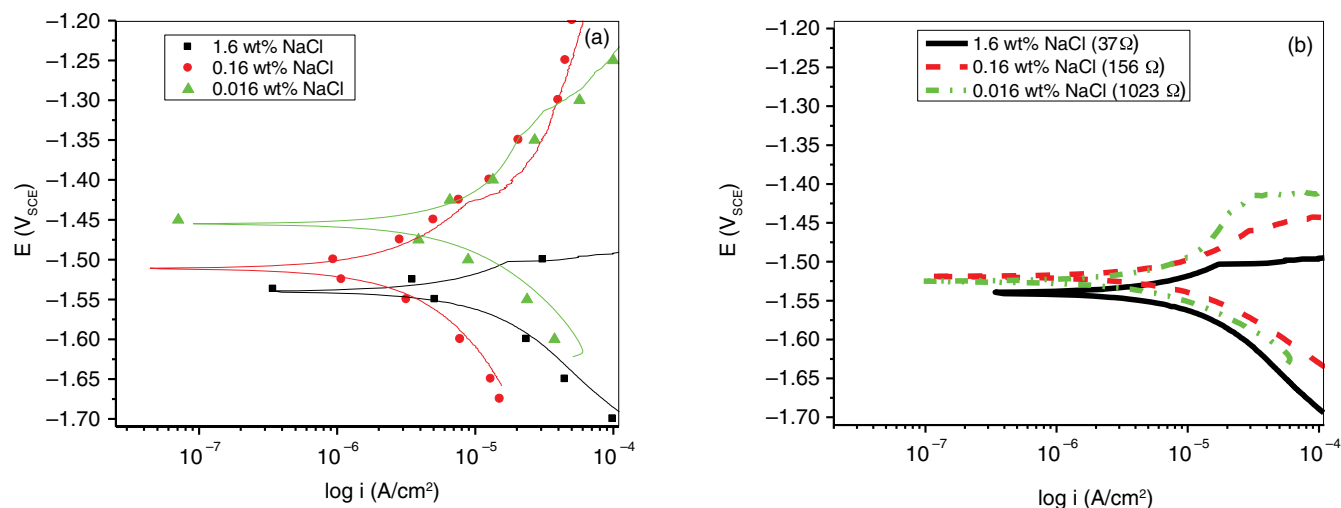
FIGURE 2. *Potentiodynamic polarization (PDP) scans (a) recorded on freshly polished ZEK100 sample at a scan rate of 0.167 mV/s following 1 h at E_{CORR} in 1.6 wt% NaCl (black), 0.16 wt% NaCl (red), 0.016 wt% NaCl (green). The scatter points are the average reading from the PDP scans at each concentration; (b) iR compensated polarization curves.*

Intermittent Immersions in Chloride Solutions

Figure 3 shows SEM micrographs of the heavily damaged ZEK100 surface following two consecutive 24 h immersions in 1.6 wt% NaCl. Because of the extensive corrosion, 1.6 wt% NaCl is too aggressive a solution to allow study of the behavior of the micro-structural constituents. A 0.16 wt% NaCl solution was, therefore, used in subsequent experiments.

The evolution of the E_{CORR} measured on ZEK100 over two 24-h immersions in 0.16 wt% NaCl is shown in Figure 4. During the first immersion, E_{CORR} rose rapidly over the first 2 h to –1.57 V, and then steadily increased to –1.55 V after 24 h. The noise associated with the measurement is likely due to the localized attack of the ZEK100 sample. After 24 h, the sample was removed for further analysis of the AOI. On re-immersion, E_{CORR} again rose rapidly to –1.45 V at 27 h. The subsequent sharp drop in E_{CORR} at 27 h likely indicates the re-establishment of active conditions, possibly due to the breakdown of a thin oxide formed on air exposure between the two immersion periods.

Figure 5 shows the corroded ZEK100 surface after the two 24-h immersion periods (Figure 4). SEM micrographs of the polished ZEK100 surface are shown in Figures 5(a) and (d). The arrows in Figure 5(a) indicates the location of two particles, which act as reference points when reviewing the area after corrosion. Following 24 h of immersion in the 0.16 wt% NaCl solution, the AOI was again located and SEM micrographs are shown in Figures 5(b) and (e). Corrosion damage was observed to track laterally along the rolling direction of the alloy. Following the second 24-h immersion period, the corrosion damage was still predominantly associated with areas of initial attack, but had extended slightly into the α-matrix, Figures 5(e) and (f).
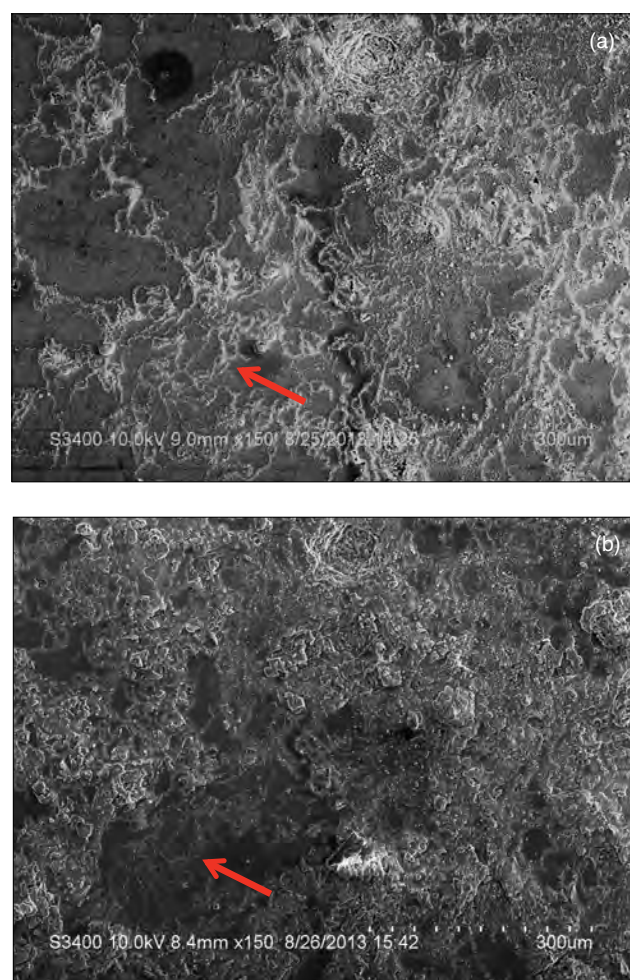

FIGURE 3. *SE SEM micrographs of a ZEK100 sample following (a) 24 h, and (b) 48 h of immersion in a 1.6 wt% NaCl solution. The arrow (red) indicates the same location in both images.*

A magnified view of the resulting damage morphology on the surface is seen in the SEM micrographs in Figure 6. Figure 6(a) shows a corroded region covered with protruding corrosion product following 48 h of immersion in 0.16 wt% NaCl. When the corrosion product was removed, Figure 6(b), the damage was seen to have propagated laterally along the surface, possibly by the coalescence of pits as previously claimed for the ZE41 alloy.[30] Some general, but shallow, damage occurred on the top surfaces, which remained generally intact. Figure 6(c) shows that corrosion penetration into the alloy was limited to a depth between 2 μm and 5 μm and occurred primarily in the center of these tracks.

The corrosion of Mg alloys is strongly supported by microgalvanic coupling to secondary phases and it has been suggested that active cathodes can be identified by their tendency to accumulate corrosion product domes of magnesium hydroxide ($Mg(OH)_2$).[24] Figure 7(a) shows such a corrosion product dome at the site denoted with an arrow (green) in Figures 5 (d), (e), and (f), located within a corroded region following 48 h of corrosion in 0.16 wt% NaCl. When the corrosion product was removed, the particles on which it had accumulated could be seen, Figure 7(b). XEDS mapping shows the presence of two Zn-Nd particles (labelled 1 and 2), Figures 7(c) and (d), and a Zr particle contaminated with Fe (labelled 3), Figures 7(e) and (f).

Short-term immersions in the 0.16 wt% NaCl solution yielded further insight into the function of ac-
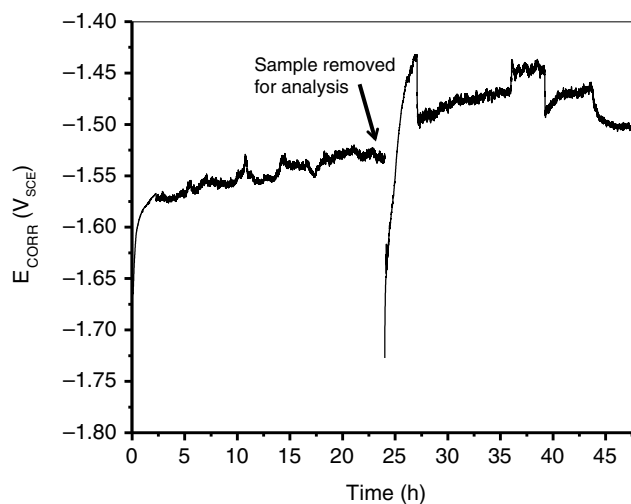
tive cathodes in the early stages of corrosion as shown in Figure 8. Figure 8(a) shows two particles located on the ZEK100 surface prior to immersion. The small particle on the left is Zr, as identified in the XEDS map of Zr, Figure 8(c), and no Fe can be detected in this particle, Figure 8(d). However, a weak Zn signal is observed from this particle, Figure 8(f)—a possible Zn-
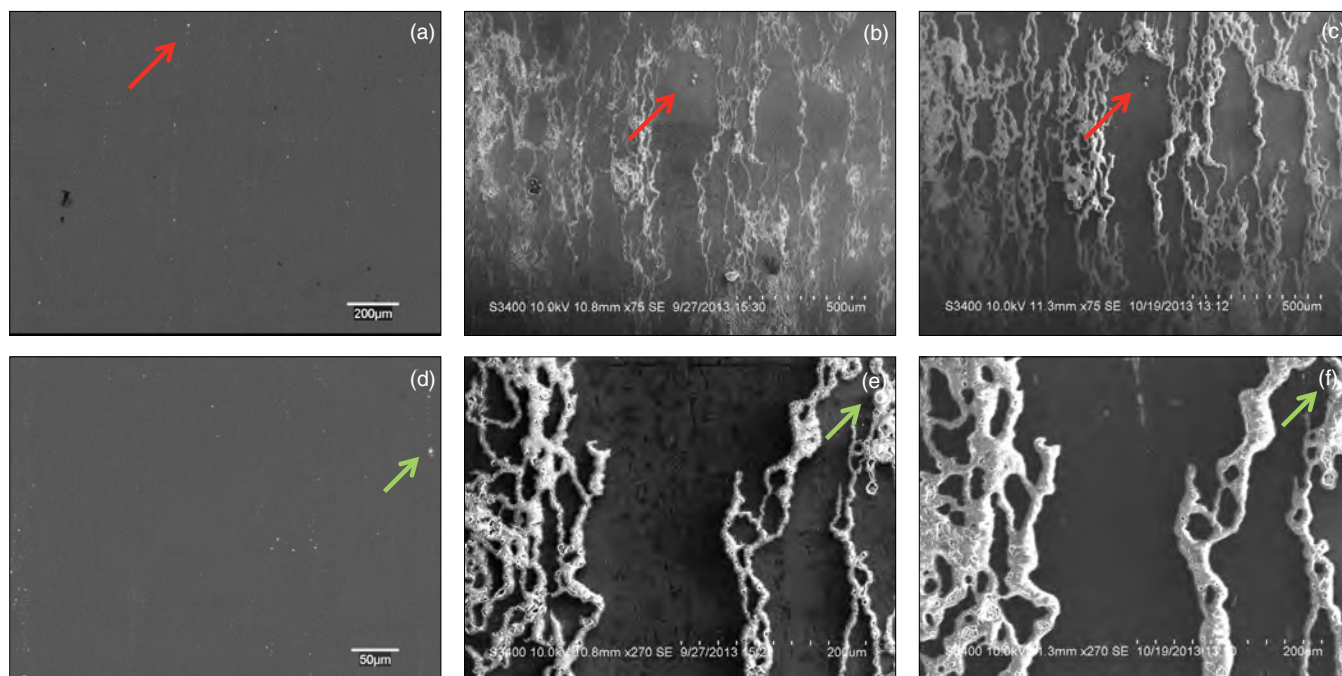

FIGURE 4. *Evolution of E_{CORR} recorded on a ZEK100 sample in a 0.16 wt% NaCl solution. After 24 h the sample was removed for analysis, and then reimmersed in a new solution for an additional 24 h period.*

FIGURE 5. *SEM micrographs of a selected AOI on a ZEK100 sample: (a) and (d) original polished surface: (b) and (e) after 24 h of immersion, and (c) and (f) after 48 h of immersion in a 0.16 wt% NaCl solution. The arrows (red) in (a), (b), and (c) identify two particles that are reference points in the AOI. The arrows (green) in (d), (e), and (f) identify the domed structure analyzed in Figure 7.*
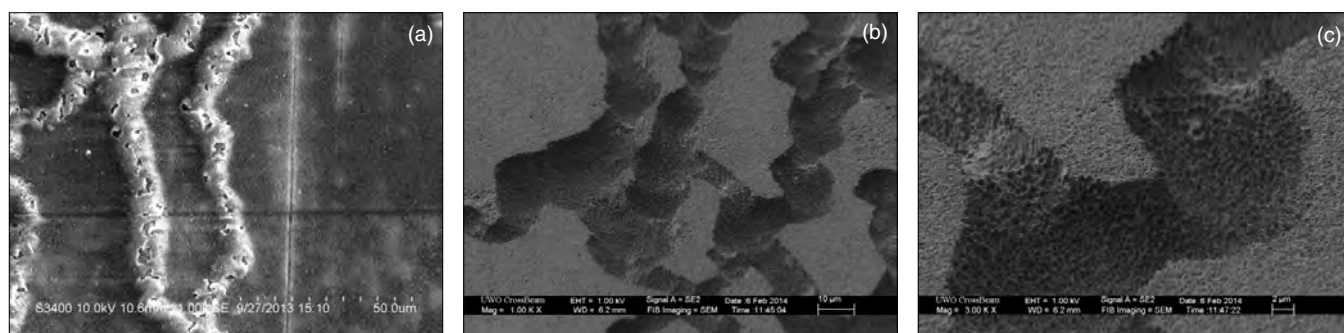
FIGURE 6. *SE SEM micrographs of the ZEK100 sample surface after 48 h of immersion in a 0.16 wt% NaCl solution showing (a) the regions filled with corrosion product, (b) these regions following removal of the corrosion product; (c) a magnified image of a corroded region.*

Zr phase observed previously on ZE10A.[19] This was the sole instance of such a particle being observed in the course of this study. The larger particle on the right contains Nd [Figure 8(e)], and Zn [Figure 8(f)], and minor amounts of Fe [Figure 8(d)]. Re-examination after 6 h of immersion in 0.16 wt% NaCl showed that neither of these particles, the Zn-Nd or the Zn-Zr, accumulated a dome of corrosion product indicating very low cathodic activity, Figure 9(a). One of these domes, which is highlighted with a box (red) in Figure 9(b) was selected for XEDS mapping and shown in a magnified view in Figure 9(c). XEDS mapping of this area revealed Zr, Figure 9(e) and Fe, Figure 9(f), located below the accumulated corrosion product. The weak Mg signal from the dome structure, Figure 9(d), which is composed of magnesium oxide (MgO)/ $Mg(OH)_2$,[24] can be attributed to the low density of the corrosion product, and the comparative strength of the Mg signal from the adjacent alloy surface.

Intermittent Immersions in Pure Water

To avoid the extensive propagation of corrosion damage, a series of consecutive exposures to deionized water were conducted over a total exposure pe-
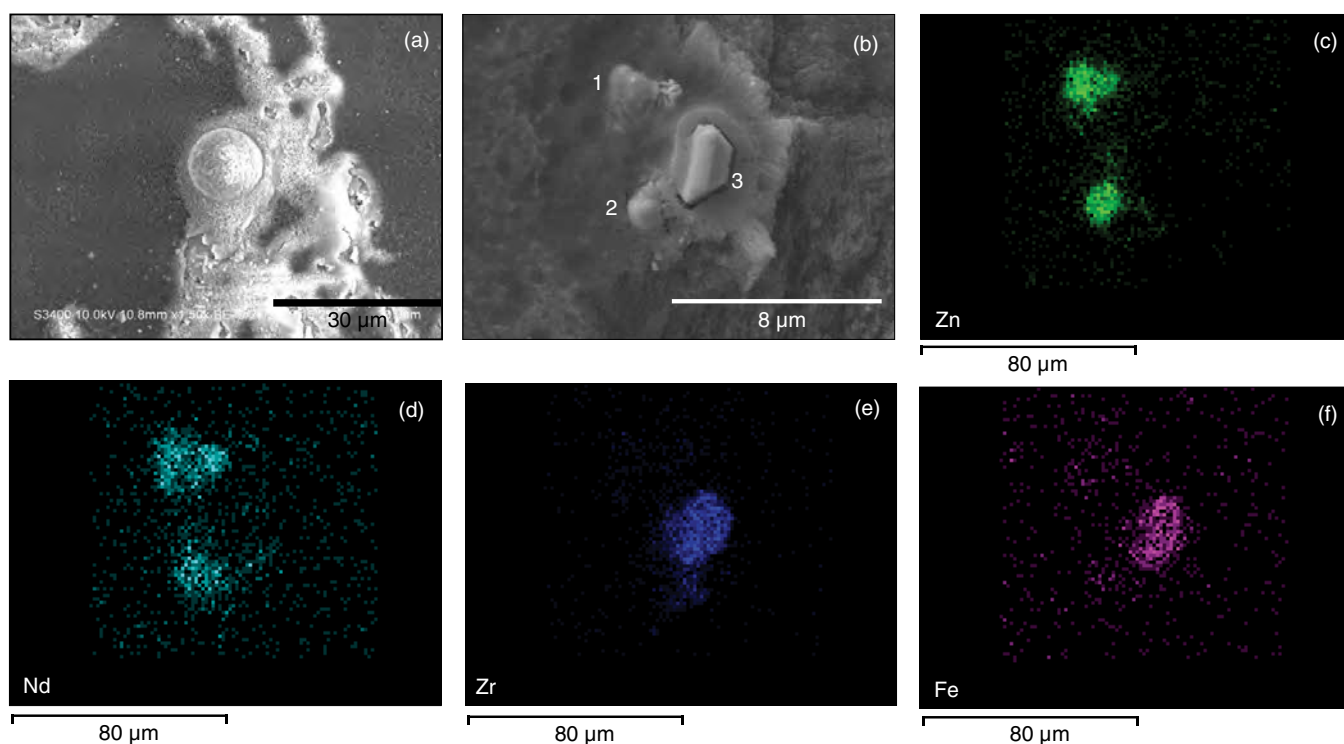

FIGURE 7. *SE SEM micrograph of (a) a corrosion product dome present on the ZEK100 sample (at the locations indicated by the arrow [green] in Figure 5[d], [e] and [f]) after 48 h of corrosion in a 0.16 wt% NaCl solution; (b) this location following removal of the corrosion product showing the particles beneath the deposit: XEDS maps for (c) Zn, (d) Nd, (e) Zr, (f) Fe.*
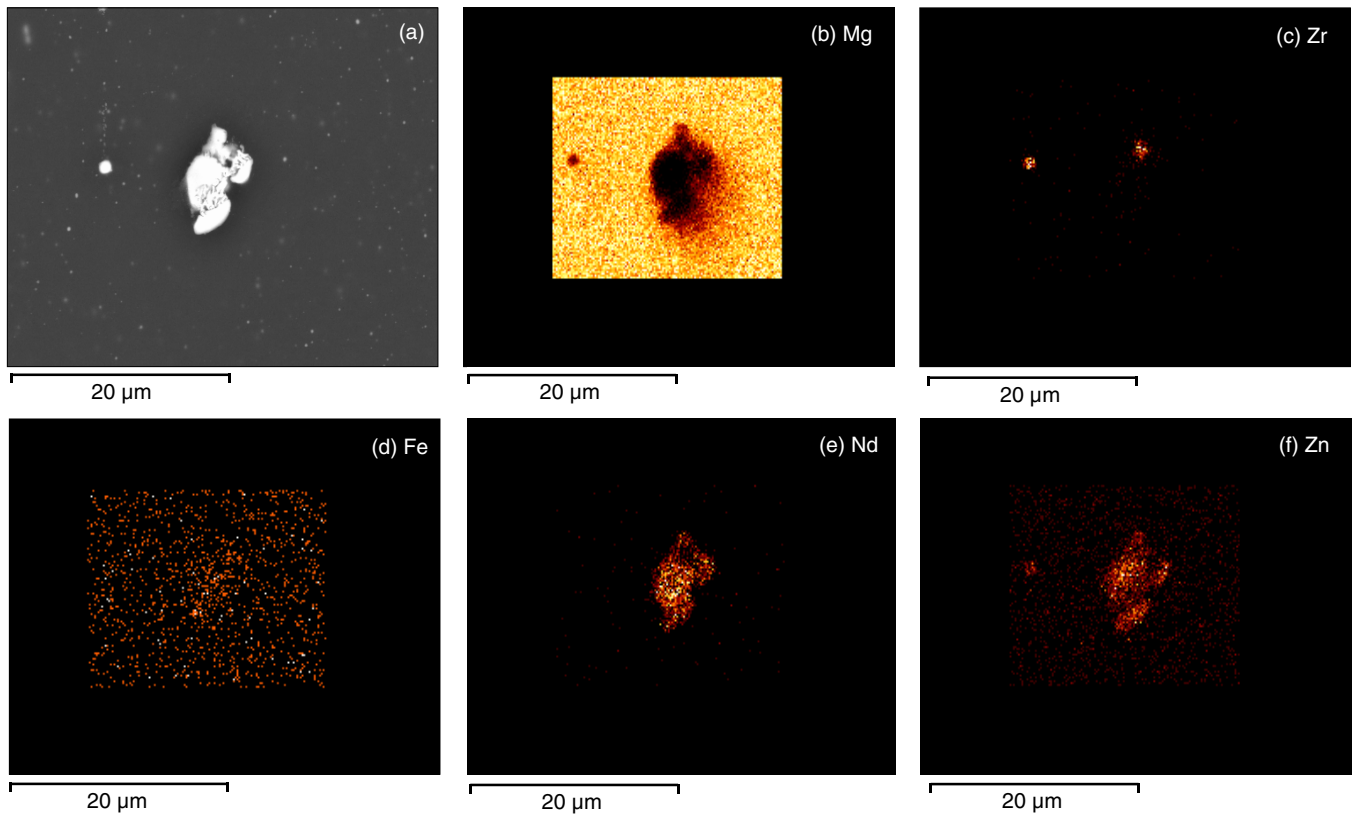
FIGURE 8. *(a) BSE SEM image of two particles on the ZEK100 surface prior to corrosion and the corresponding XEDS maps for (b) Mg, (c) Zr, (d) Fe, (e) Nd, (f) Zn.*
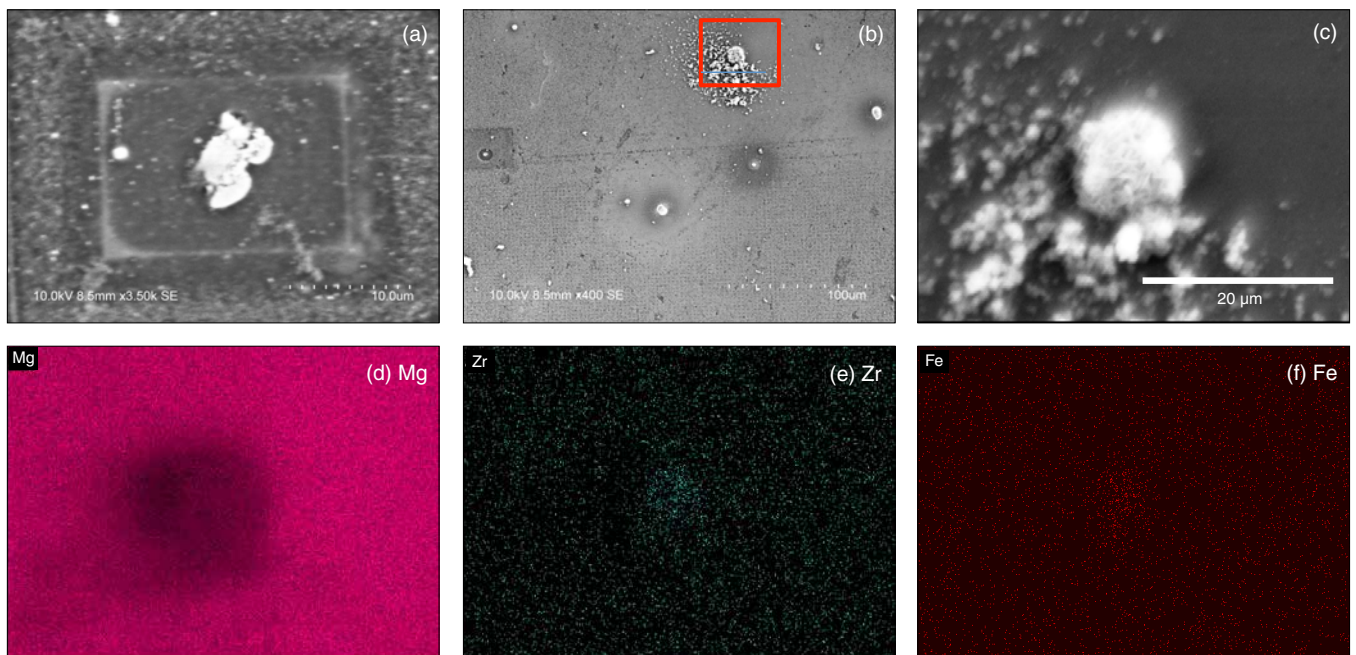

FIGURE 9. *(a) SE SEM micrograph of the particles shown in Figure 8 following 6 h of immersion in a 0.16 wt% NaCl solution, (b) SE SEM micrograph of the cathodic sites on the same sample after 6 h of immersion, (c) dome of corrosion product indicating cathodic behavior of the particle shown in the box (red) in (b); and the corresponding XEDS maps of the site for (d) Mg, (e) Zr, (f) Fe.*

riod of 192 h, Figure 10. Within the selected AOI after 24 h of immersion, Figure 10(a), three distinct inter-metallic particles were recognizable as bright spots. These particles were covered with corrosion product domes indicating cathodic activity, as shown for the bottom particle labeled with an arrow (red) in Figure 10(a), Figure 10(e). As expected, very little damage to the bulk surface was observed, and no evidence for the tracking of corrosion across the surface was observed. After 48 h of immersion, the general surface displayed minor accumulation of corrosion product, Figure 10(f), while after 96 h of immersion, more significant morphological changes were observed, Figures 10(c) and (g). Rings of corrosion damage, located around the particles, and slight cracking of the corrosion product at the outer edges of these regions had occurred. The general surface developed some topographical texture as corrosion product accumulated over the whole surface. After 192 h of immersion, sufficient corrosion product had accumulated on the surface for cracks to appear when the sample was removed from the cell and dried. The corrosion product domes remained intact over the particles. In addition, there was no clear evolution in either the size or morphology of the particle shown in Figures 10(e) through (h) suggesting the corrosion product dome formed rapidly and did not grow as corrosion progressed.

Figure 11(a) shows a BSE SEM micrograph of the ZEK 100 surface following 192 h of immersion in water. Figures 11(b) through (f) show the corresponding XEDs graphs for Zn, Nd, Zr, and O. The two particles located in the top right corner of the images had accumulated corrosion product domes indicating cathodic activity, while the majority of particles on the surface had not. A magnified view of the particles located within the box (red) in Figure 11(a) is shown in the SEM micrograph in Figure 11(b), and XEDS analyses show the presence of Zn and Nd, Figures 11(c) and (d). Additionally, this area is free of Zr, Figure 11(e). The absence of any enhanced XEDS signal for O on these particles compared to the surrounding surface was consistent with the absence of any corrosion product deposits. Analysis of a separate particle on the surface, also free of corrosion product, Figure 11(g), showed it to be Zr, Figure 11(h), with no detectable Fe content, Figure 11(i).

A particle, which did accumulate a corrosion product dome following 192 h of exposure in water, Figure 12(a) was FIB cross-sectioned. A cracked ring of corrosion damage was visible surrounding the particle. At a location 0.25d in from the edge of the dome (d is the diameter of the dome), damage had penetrated up to 4 μm to 5 μm into the alloy and the corroded location was filled with dense corrosion product, Figure 12(b). At 0.45d, a second damaged location was detected, Figure 12(c). The maximum height of the dome was ~8 μm to 10 μm compared with a general depth of corrosion product of 1 μm to 2 μm on the adjacent surface just beyond the edge of the dome, Figure 12(c). A particle was also observed, marked with the arrow (red) in Figure 12(d), at the bridge between two corroded regions, which XEDS, Figure 12(e), showed the particle contained 53 at% Fe with 47 at% Zr.

These results show that, in the absence of chloride, corrosion damage on ZEK100 was confined to locations near active cathodic sites, while in the presence of chloride propagation tracks along the surface. The stereomicrographs in Figure 13 illustrate the differences in these general patterns. Figure 13(a) shows
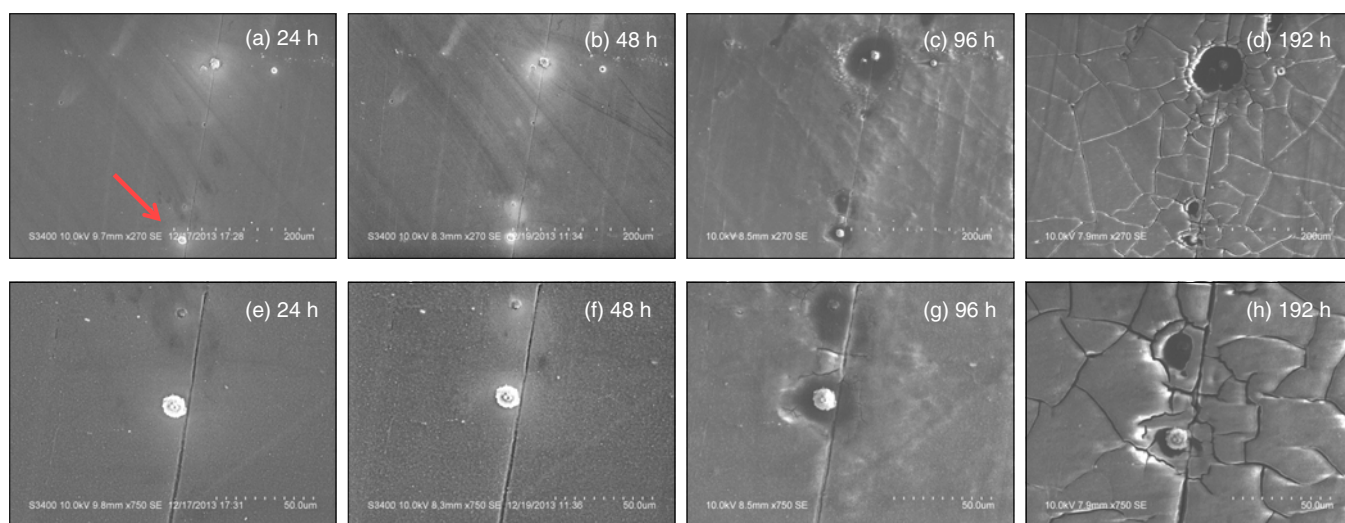

FIGURE 10. *SE SEM micrograph showing the progression of corrosion on an AOI on a ZEK100 sample in deionized water monitored by SEM showing an AOI after (a) 24 h, (b) 48 h, (c) 96 h, (d) 192 h: the progression of corrosion around the particle indicated by the arrow (red) in (a) after (e) 24 h, (f) 48 h, (g) 96 h, (h) 192 h of immersion.*
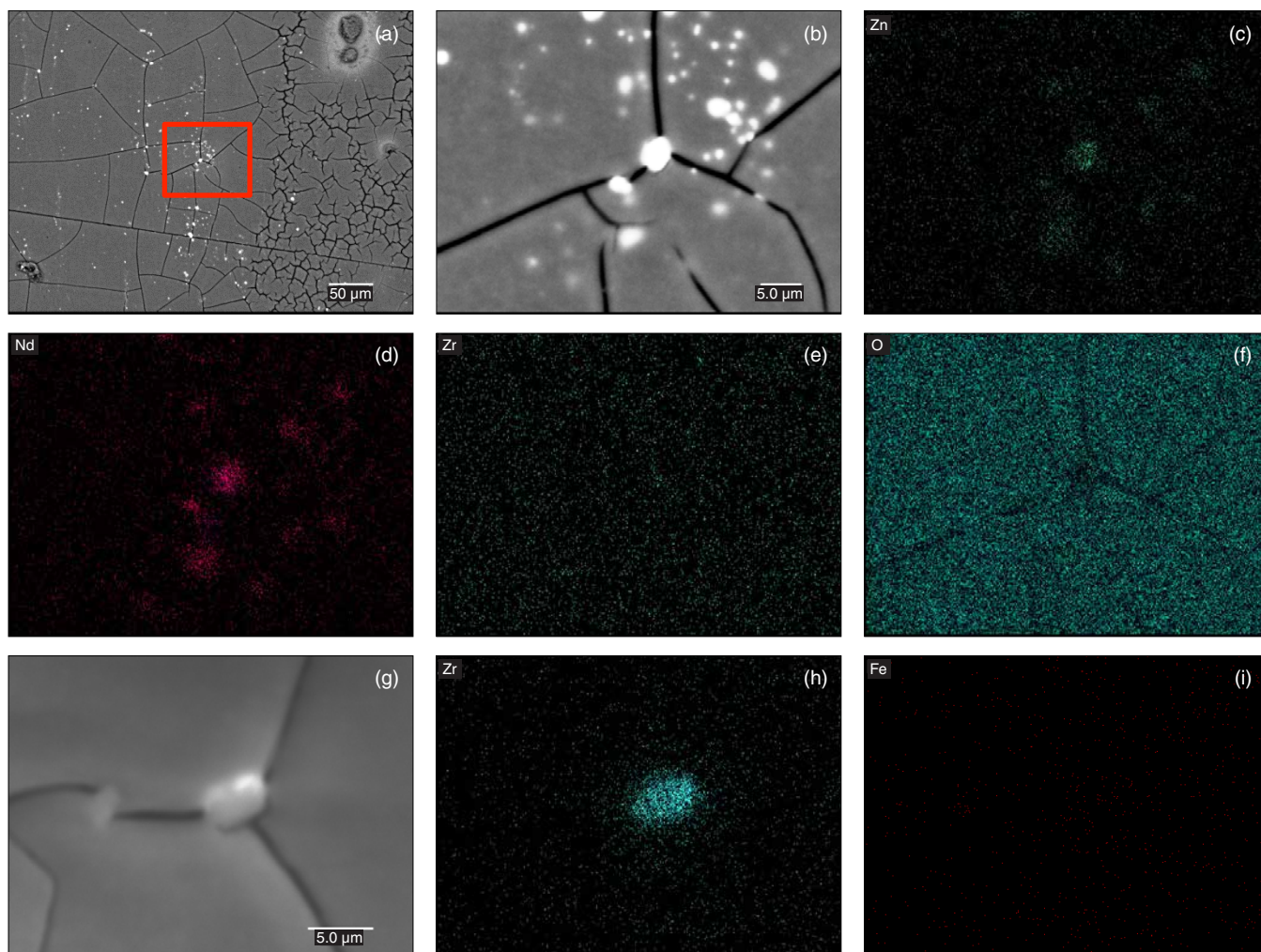
FIGURE 11. *(a) BSE SEM micrograph of the ZEK 100 surface after 192 h of immersion in water, (b) BSE SEM micrograph of the area marked with the box (red) in (a), and the corresponding XEDS maps for (c) Zn, (d) Nd, (e) Zr, and (f) O, (g) SE SEM micrograph of a separate particle on the ZEK100 surface and the corresponding XEDS maps for (h) Zr and (i) Fe.*

the ZEK100 surface following 24 h of exposure in 0.16 wt% NaCl when corrosion can be seen to have tracked along the alloy surface. By contrast, in the absence of chloride, Figure 13(b), damage remains isolated near secondary phases on the ZEK100 surface. Additionally, the bright spots in Figure 13(b) clearly show the general distribution of overlapping zones of corrosion linking closely located particles, identified by the white arrow. Additionally, of the particles available on the alloy surface, only a relatively small fraction have stimulated microgalvanic corrosion in water.

DISCUSSION

The microstructure of the ZEK100 alloy contained Zr intermetallic particles and Zn-Nd containing particles, most likely a T-phase (Mg-Zn-Nd), was widely dispersed within the α-Mg matrix. A Zn-Zr particle was also identified in the study. The Mg-Zn-

Nd phase, which has been shown to be present in the ZE41 alloy,[29-30] was observed as discrete particles in the ZEK100, in contrast to the extended T-phase ligaments along the grain boundaries observed in the ZE41—an alloy with higher contents of RE and Zn.

As observed previously for the ZE41 alloy, the rate and extent of corrosion decreased as the chloride concentration decreases. The PDP curves in Figure 2 show this was predominantly an anodic effect, the cathodic kinetics of water reduction being only marginally influenced. In 1.6 wt% NaCl, protection from corrosion by a surface film was marginal, rapid breakdown being observed at potentials only a few millivolts anodic of E_{CORR}, Figure 2. This inability to provide protection was confirmed by the SEM micrographs in Figure 3, which show generally distributed corrosion damage after 24 h and 48 h of exposure to this solution.

Reducing the chloride concentration to 0.16 wt% extended the partially protective properties of the film
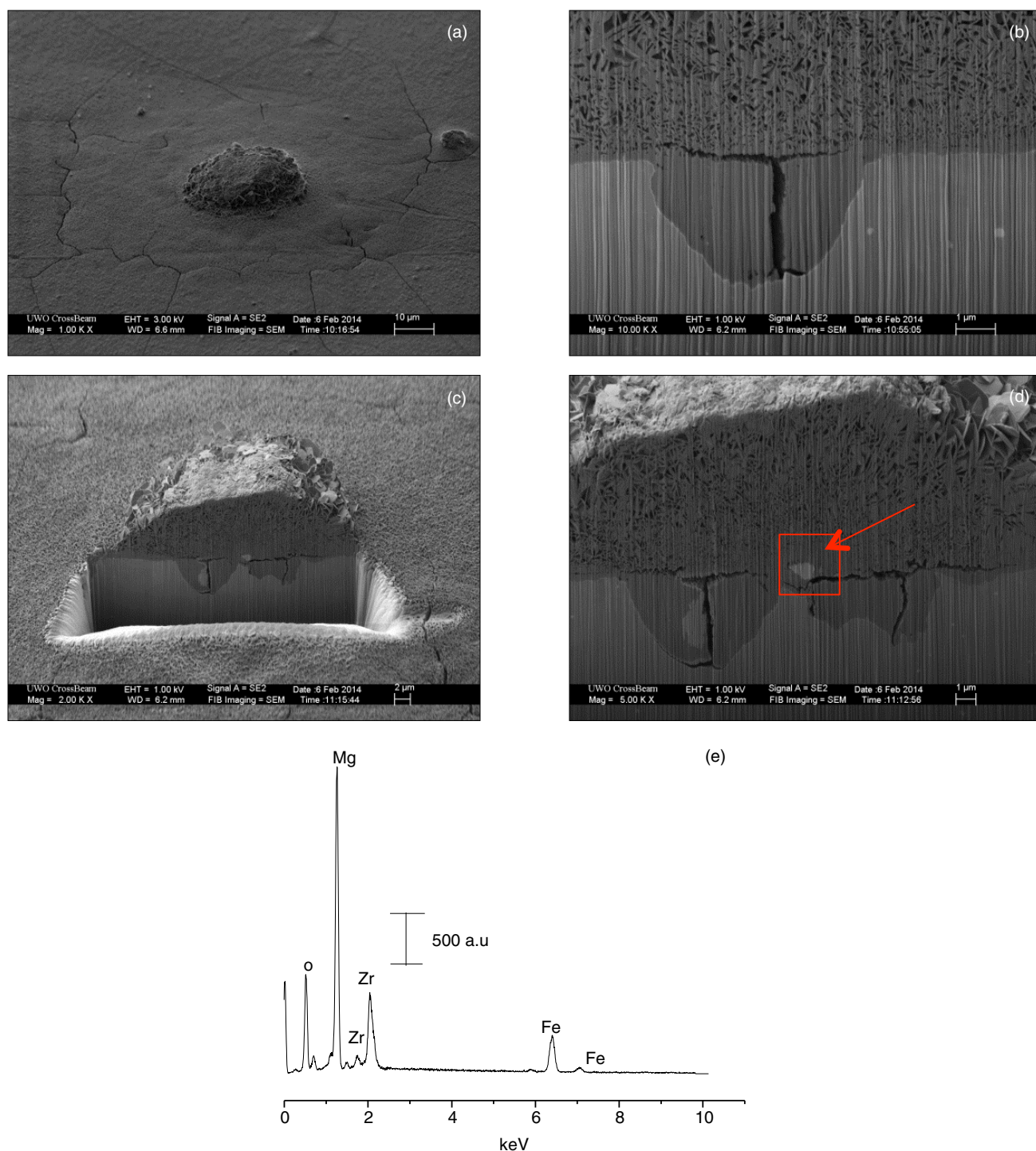
FIGURE 12. *(a) SE SEM micrograph of a corrosion product dome on the surface of the ZEK100 sample after 192 h of immersion in deionized water: (b) SE SEM micrograph of a FIB cross at ¼ depth into the dome, (c) FIB cross section at a location deeper into the dome; (d) SEM image revealing a particle below the corrosion product dome marked with the arrow (red), (e) XEDS spectrum of the region highlighted in (d) with a box (red).*

to ~ −1.45 V, and a further reduction to 0.016 wt% to ~ −1.40 V. Confirmation of the chloride effect in the PDP scans was observed through iR-compensation.[31] The E_{CORR} measured during exposure to 0.16 wt% NaCl was generally below the breakdown potential

measured in the PDP scan although it steadily increased with rapid fluctuations towards this value, −1.45 V, over the two 24-h exposure periods. Commonly, an unstable E_{CORR} that is less than the film breakdown potential would indicate metastable lo-
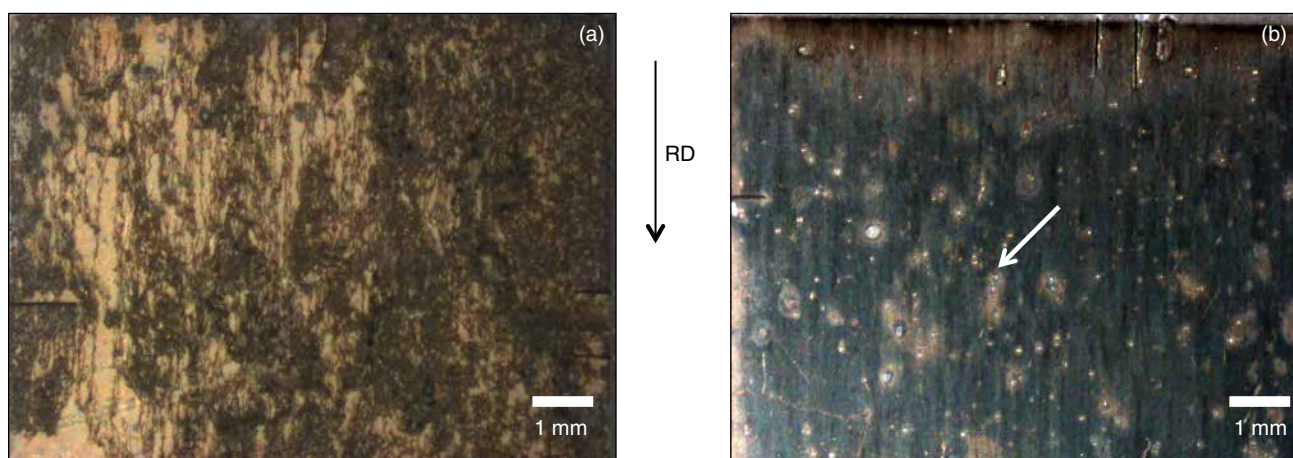
FIGURE 13. *Stereo micrographs comparing the general corrosion damage on the ZEK100 sample following (a) 24 h of exposure in 0.16 wt% NaCl; and (b) 192 h of exposure in deionized water. The rolling direction (RD) of the samples is indicated by the black arrow and the white arrow shows overlapping regions of corrosion damage.*

calized corrosion. Consistent with this expectation, general corrosion of the surface was not observed, corrosion damage being restricted to tracks along the surface in a filiform-like manner, common for Mg systems.[22,32] The increase in E_{CORR} with time then reflected the increased area of the surface exposed.

Corrosion, preferentially within grain boundaries, has been reported previously for Mg-Zn-RE alloys and is attributed to the presence of the T-phase in the boundaries and the depletion of alloying elements at grain boundaries housing this phase.[29] In the ZK60 alloy, containing Zn and Zr without REs, grain boundary attack was linked to the presence of Mg-Zn precipitates and the depletion of Zn in the grain boundary region.[33] Similar grain boundary depletion could account for the distribution of damage observed here on the ZEK100 alloy, with the tracks of corrosion damage interlinking the secondary phase particles spread throughout the alloy. An alternative possibility would be that damage initiated along the [0001] basal plane, as suggested for pure Mg,[22] and then tracked in the prismatic direction, accounting for the progression of damage along the rolling direction of the material.

The presence and distribution of Zr has been shown to significantly influence the corrosion kinetics of Mg alloys through the size and distribution of Zr particles. When finely distributed, these particles appeared to produce a more robust and protective oxide.[34-35] However, it has been claimed that, because of their nobility,[36] Zr particles can accelerate cathode kinetics[37] leading to deep corrosion in regions with higher Zr content.[30] In Mg-Zr-Mn systems, Zr in Mg solid solution was reported to be an anodic activator of the Mg matrix, while Zr particles enhanced cathodic kinetics.[38] In the ZEK100, Zr and Nd together are added as grain refiners with the general claim that Zr has a negative effect on corrosion, while Nd reduces the cathodic activity of the phase which hosts it.[39]

In the presence of chloride, both Mg-Zn-Nd and Zr, particles were located in the corroded region with Zr particles containing Fe appearing to be the dominant microgalvanically coupled cathodes. By initiating corrosion in pure water, it was possible to limit the extent of corrosion damage due to microgalvanic coupling to the vicinity of the coupled cathodes. Over the 192-h total exposure period employed in these experiments, minimal general corrosion damage occurred, only 1 μm to 2 μm of corrosion product accumulating on the alloy surface, leading to the cracks observed upon removing the electrode from the cell and drying it. In addition, small zones of corrosion around intermetallic particles enabled functioning cathodes to be identified from inert particles.

While Zn-Nd particles were clearly identified on the alloy surface following immersion in water, they did not accumulate corrosion product deposits or small encircling corrosion zones, indicating they were generally inactive. In addition, many Zr particles were identified, but only those containing Fe were observed to accumulate the corrosion product confirming their strong cathodic activity. These observations were consistent with those made in the chloride solution, and demonstrate that the dominant cathodes are the Fe-contaminated Zr particles. This is a similar observation to the Zr particles responsible for cathodic behavior in the WE43 Mg alloy.[40] Based on these observations and the available published literature, limiting the size and controlling the distribution and purity of Zr particles would be an effective way to mitigate microgalvanically coupled cathodic behavior.

While chloride is well known to enhance localized corrosion on passive alloys as described in the point defect model,[41] this is unlikely to be the key effect on the ZEK100 alloy because Mg alloys can never be considered passive in aqueous environments. Grain boundaries in Mg-Zn-RE-Zr systems have been noted

to be depleted in Zn[33] and would be expected to be the locations most anodically susceptible; this in a similar manner to Al-depleted areas on the surface of AM50 alloys, which experienced the highest degree of corrosion.[42] Given the wide dispersion and close proximity of particles in ZEK100 alloys, even the limited reactivity of Mg in pure water might have been expected to lead to corrosion tracking along the surface. However, if active cathodes are limited to a smaller number of widely separated Zr/Fe particles, then this would prove difficult, as indicated in Figure 13, which shows no tracking corrosion and only minor interlinking of corroded locations, at least on the limited time scale of these experiments. As heavy damage was observed in the highest concentrated chloride solution, tracking damage linking the secondary microstructures was observed with lowered chloride concentration and centralized damage around the strongest cathodes in water—the more likely result of decreasing chloride content is a reduced ability of cathodes to microgalvanically couple over a long range on the alloy surface.

SUMMARY

❖ The roles of the microstructural features in the corrosion of the ZEK100 Mg alloy were investigated. The microstructure of the ZEK100 was mainly composed of a Mg-Zn-Nd phase and Zr-rich particles within the α-Mg matrix.

❖ The severity of corrosion damage was shown to depend on the chloride concentration. In concentrated solutions, corrosion damage was general and universally distributed across the alloy surface. At lower concentrations, damage was confined to lateral tracks along the surface, generally in the rolling direction. The tracking damage appeared to interlink the secondary phases of the alloy, many of which supported corrosion by acting as microgalvanically coupled cathodes. Decreasing the chloride content influences the extent and morphology of corrosion damage, likely through reducing the ability of cathodes to microgalvanically couple over longer distances on the alloy surface.

❖ Four distinct types of secondary microstructural features were identified and characterized; the Mg-Zn-Nd (T-phase), Zn-Zr, Zr, and Fe-containing Zr. Of these, the Fe-containing Zr was the most active cathode sustaining water reduction. This was most clearly shown in corrosion experiments in pure water, when the lack of solution conductivity confined corrosion to a small region in the vicinity of the active cathodes.

ACKNOWLEDGMENTS

REFERENCES

1. J. Hirsch, T. Al-Samman, *Acta Mater.* 61 (2013): p. 818-843.
2. M.K. Kulecki, *Int. J. Adv. Manuf. Tech.* 39 (2008): p. 851-865.
3. B-C. Suh, M-S. Shim, K.S. Shin, N.J. Kim, *Scripta Mater.* 84-85 (2014): p. 1-6.
4. J. Min, L.G. Hector, Jr., J. Lin, J.T. Carter, *J. Mater. Eng. Perf.* 22 (2013): p. 3324-3336.
5. E. Ghali, W. Dietzel, K. Kainer, *J. Mater. Eng. Perform.* 22 (2013): p. 2875-2891.
6. G. Song, A. Atrens, X. Wu, B. Zhang, *Corros. Sci.* 40 (1998): p. 1769-1791.
7. G. Song, Z. Xu, "The Surface," *Corros. Sci.* 55 (2010): p. 4148-4161.
8. T. Kawamura, S. Sunada, H. Notoya, K. Kondo, K. Majima, *J. Japan. Inst. Metals,* 72 (2008): p. 216-223.
9. H. Matsubara, Y. Ichige, K. Fujita, H. Nishiyama, K. Hodouchi, *Corros. Sci.* 66 (2013): p. 203-210.
10. D. Sachdeva, *Corros. Sci.* 60 (2012): p. 18-31.
11. W. Liu, F. Cao, A. Chen, L. Chang, J. Zhang, C. Cao, *Corrosion* 68 (2012).
12. H. Martin, R. Alvarez, J. Danzy, M. Horstemeyer, P. Wang, *Corrosion* 68 (2012): p. 571-585.
13. W. Song, H. Martin, A. Hicks, D. Seely, C. Walton, W. Lawrimore II, P. Wang, M. Horstemeyer, *Corros. Sci.* 78 (2014): p. 353-368.
14. T. Huehnerschulte, N. Angrisani, D. Rittershaus, D. Bormann, H. Windhagen, A. Meyer-Lindenberg, *Materials* 4 (2011): p. 1144-1167.
15. H. Waizy, A. Weizbauer, C. Modrejewski, F. Witte, H. Windhagen, A. Lucas, M. Kieke, B. Denkena, P. Behrens, A. Meyer-Lindberg, F.W. Bach, F. Thorey, *Biomed. Eng. Online* 11 (2012): p. 1-14.
16. D. Dziuba, A. Meyer-Lindberger, J. Seitz, H. Waizy, N. Angrisani, J. Reifenrath, *Acta Biomater.* 9 (2013): p. 8548-8560.
17. M.L. Nascimento, C. Fleck, W.D. Muller, D. Lohe, *Int. J. Mat. Res.* 97 (2006): p. 1586-1595.
18. T. Cain, L.G. Bland, N. Birbilis, J.R. Scully, "A Compilation of Corrosion Potentials for Magnesium Alloys," *Corrosion* (2014), in-press.
19. K.A. Unocic, H.H. Elsentriecy, M.P. Brady, H.H. Meyer III, G.L. Song, M. Fayek, R.A. Melsner, B. Davis, *J. Electrochem. Soc.* 161 (2014): p. C302-C311.
20. M.P. Brady, M. Fayek, H.H. Elsentriecy, K.A. Unocic, L.M. Anovitz, J.R. Keiser, G.L. Song, B. Davis, *J. Electrochem. Soc.* 161 (2014): p. C395-C404.
21. R.M. Asmussen, W.J. Binns, P. Jakupi, D. Shoesmith, *J. Electrochem. Soc.* 161 (2014): p. C501-C508.
22. G. Williams, H. ap Llwyd Dafydd, R. Grace, *Electrochim. Acta* 109 (2013): p. 489-501.
23. G. Williams, R. Grace, R.M. Woods, *Corrosion* (2014), in-press. http://dx.doi.org/10.5006/137624.
24. M. Danaie, R.M. Asmussen, P. Jakupi, D.S hoesmith, G. Botton, *Corros. Sci.* 83 (2014): p. 299-309.
25. N. Birbilis, G. Williams, K. Gusieva, A. Samaniego, M.A. Gibson, H.N. Murray, *Electrochem. Commun.* 34 (2013): p. 295-298.
26. N. Birbilis, A.D. King, S. Thomas, G.S. Frankel, J.R. Scully, *Electrochim. Acta* 132 (2014): p. 277-283.
27. G. Williams, N. Birbilis, H.N. McMurray, *Electrochem. Commun.* 36 (2013): p. 1-5.
28. M. Taheri, J.R. Kish, N. Birbilis, M. Danaie, E.A. McNally, J.R. McDermid, *Electrochim. Acta* 116 (2014): p. 396-403.
29. A. Coy, F. Viejo, P. Skeldon, G. Thompson, *Corros. Sci.* 52 (2010): p. 3896-3906.
30. W. Neil, M. Forsyth, P. Howlett, C. Hutchinson, B. Hinton, *Corros. Sci.* 51 (2009): p. 387-394.
31. A.D. King, N. Birbilis, J.R. Scully, *Electrochim. Acta* 121 (2014): p. 394-406.

32. P. Schmutz, V. Guillaumin, R.S. Lillard, J.A. Lillard, G.S. Frankel, *J. Electrochem. Soc.* 150 (2003): p. B99-B110.
33. R. Zeng, K.U. Kainer, C. Blawert, W. Dietzel, *J. Alloys Compd.* 509 (2011): p. 4462-4469.
34. G. Ben-Hamu, D. Eliezer, K.S. Shin, S. Cohen, *J. Alloys Compd.* 431 (2007): p. 269-276.
35. J.W. Chang, X.W. Guo, P.H. Fu, L.M. Peng, W, J. Ding, *Trans. Nonferrous Metals Soc. China* 17 (2007): p. 1152-1157.
36. M. Sun, G. Wu, W. Wang, W. Ding, *Mat. Sci. Eng. A* 523 (2009): p. 145-151.
37. D. Gandel, M. Easton, M. Gibson, T. Abbott, N. Birbilis, *Corros. Sci.* 81 (2014): p. 27-35.
38. D. Gandel, M. Easton, M. Gibson, N. Birbilis, *Corrosion* (2013): p. 744-751.
39. J. Chang, J. Duo, Y. Xiang, H. Yang, W. Ding, Y. Peng, *Int. J. Miner., Metall. Mater.* 18 (2011): p. 203-209.
40. M. Ascencio, M. Pekguleryuz, S. Omanovic, *Corros. Sci.* 87 (2014): p. 489-503.
41. L.F. Lin, C.Y. Chao, D.D. Macdonald, *J. Electrochem. Soc.* 128 (1981): p. 1194-1198.
42. R.M. Asmussen, P. Jakupi, M. Danaie, G. Botton, D.W. Shoesmith, *Corros. Sci.* 75 (2013): p. 114-122.